Advanced Energy Materials

ADVANCED ENERGY MATERIALS
www.advenergymat.de

RESEARCH ARTICLE OPEN ACCESS

How Particle Size Affects Consolidation Behavior, Strain and Properties of Li_6PS_5Cl Fast Ionic Conductors

Vasiliki Faka[1] | Mohammed Alabdali[2,3] | Martin A. Lange[1,4] | Franco M. Zanotto[2,3] | Can Yildirim[5] | Mikael Dahl Kanedal[6,7] | Jędrzej Kondek[1,8,9] | Matthias Hartmann[1,8] | Oliver Maus[1,8] | Dominik Daisenberger[10] | Michael Ryan Hansen[9] | Jozef Keckes[11,12] | Daniel Rettenwander[6,7,13] | Alejandro A. Franco[2,3,14,15] | Wolfgang G. Zeier[1,4]

[1]Institute of Inorganic and Analytical Chemistry, University of Münster, Münster, Germany | [2]Laboratoire De Réactivité Et De Chimie des Solides, UMR CNRS 7314, Université de Picardie Jules Verne, Amiens, France | [3]FR CNRS 3459, Réseau sur le Stockage Electrochimique de l'Energie (RS2E), Hub de l'Energie, Amiens, France | [4]Institute of Energy Materials and Devices (IMD), IMD 4: Helmholtz-Institut Münster Ionics in Energy Storage, Forschungszentrum Jülich GmbH, Münster, Germany | [5]European Synchrotron Radiation Facility, Grenoble, France | [6]Department of Material Science and Engineering, NTNU Norwegian University of Science and Technology, Trondheim, Norway | [7]Christian Doppler Laboratory For Solid-State Batteries, NTNU Norwegian University of Science and Technology, Trondheim, Norway | [8]International Graduate School BACCARA, Münster, Germany | [9]Institute of Physical Chemistry, University of Münster, Münster, Germany | [10]Harwell Science and Innovation Campus, Diamond Light Source, Oxfordshire, UK | [11]Erich Schmid Institute of Materials Science, Austrian Academy of Sciences, Leoben, Austria | [12]Chair of Materials Physics, Montanuniversität Leoben, Leoben, Austria | [13]Center For Transport Technologies, Battery Technologies, AIT Austrian Institute of Technology GmbH, Vienna, Austria | [14]FR CNRS 3104, ALISTORE-European Research Institute, Hub de l'Energie, Amiens, France | [15]Institut Universitaire de France, Paris, France

Correspondence: Alejandro A. Franco (alejandro.franco@u-picardie.fr) | Wolfgang G. Zeier (wzeier@uni-muenster.de)

Received: 14 September 2025 | **Revised:** 1 January 2026 | **Accepted:** 8 January 2026

Keywords: argyrodites | compression | solid electrolytes | solid-state batteries | strain

ABSTRACT

Solid-state battery fabrication requires the densification of solid electrolytes to achieve optimal cycling performance and high energy density. However, the underlying compaction mechanisms of these electrolytes remain poorly understood. Here, we investigate the effect of pressure consolidation on the ionic conductor Li_6PS_5Cl with particle size distributions (PSD) ranging from 4 to 40 µm. Heckel analysis reveals that samples with smaller PSDs exhibit higher compressibility at lower pressures. X-ray diffraction peak profiling shows that applied pressure induces lattice strain, leading to peak broadening, while pair distribution function analysis demonstrates a reduction in coherence length upon pressing. Dark-field X-ray microscopy further provides spatially resolved orientation maps, uncovering intragranular structural variations within individual Li_6PS_5Cl agglomerates after compression. To better understand the origin of stress fluctuations, we performed discrete element method simulations using the experimental PSDs. The results indicate that smaller particles and broader PSDs experience higher stresses, whereas monodisperse systems do not exhibit significant stress fluctuations with position or particle size. This suggests that the high strain observed cannot be attributed solely to smaller particles, but rather to size inhomogeneity. Overall, these findings highlight that both particle size and its distribution play a critical role in processing solid electrolytes for solid-state batteries.

Vasiliki Faka and Mohammed Alabdali contributed equally to this work.

1 | Introduction

Solid-state batteries are of high interest due to their potential high energy densities [1]. Solid electrolytes, as their main component [2], have been extensively investigated; with sulfides to be one of the most promising candidates [3]. Many efforts have focused on increasing the ionic conductivity of solid electrolytes [4, 5], needed to enable high energy densities and high-power output [6]. In solid-state systems, close contact between particles is required to generate homogeneous electric (both electronic and ionic) currents and minimize internal resistance [7]. This makes the application of pressure at different steps of the cell building process indispensable. The densification of solid electrolytes is a significant part of the cell assembly, because higher relative densities usually promise higher ionic conductivity [8]. Additionally, the densification process can significantly impact the resulting porosity, especially along the densification direction, enhancing or inhibiting cycling properties [9]. On a laboratory scale, solid electrolytes are pressed in the form of pellets to fabricate solid-state batteries [10]. The number of empty spaces (voids) existing among the solid electrolyte particles is considered unfavorable, therefore a high relative density of pellets is needed to improve particle contact [11]. High-pressure compression reduces the voids between the solid electrolyte particles, thereby forming better lithium-ion conduction pathways and enabling higher ionic conductivity [12]. A recent work from Korjus et al. [13]. reported the in situ densification of Li_6PS_5Cl, where cracking of large Li_6PS_5Cl particles was observed when applying high densifying pressures. Efforts to scale up the densification of sulfide-based solid-state battery components indicate that calendering remains the dominant industrial approach due to its robustness and high throughput; however, its applicability is constrained by particle fracture, interlayer delamination, and pronounced elastic recovery ('spring-back') at elevated line loads, as demonstrated in the Li_6PS_5Cl separator sheet study by Heck et al. [14]. These mechanically driven limitations highlight that densification window and microstructural stability become increasingly narrow at production-relevant pressures. In slurry based manufacturing, the required binder, as a non-conductive additive, can limit the ionic transport severely, since slurry processing requires relatively high polymer fractions (≈4 wt.%). Dry processing routes on the other hand, as demonstrated by Rosner et al. [15]. and Dupuy et al. [16]. enable much lower binder contents (≈0.5–1 wt.%), preserving the ion-transport network.

Previous computational modeling studies investigating solid-state composite electrodes at the mesoscale show that the optimal performance is achieved when the composite cathodes and anodes have around 30 wt. % of Li_6PS_5Cl [17, 18]. These efforts studied the influence of the particle size distribution (PSD) based on the D_{50} values without a deep analysis on the impact of the heterogeneity within the PSD of the Li_6PS_5Cl solid electrolyte. However, our previous computational study [19] shows that the ionic conductivity changes depend on the applied stress, thereby the compression stress during processing influences the final conductivity in composite electrodes. Additionally, there are no simulation studies focusing on the compaction behavior within argyrodite systems, since they are not easy to design and likely computationally expensive to simulate with high fidelity. A sole experimental fracture visualization reported with a $Li_{1+x}Al_xGe_{2-x}(PO_4)_3$ separator [20].

Experimental reports about compression under high-pressure of Li_6PS_5Cl revealed increasing contact area and sphericity of single solid electrolyte particles, suppressing the voids between and within the solid electrolyte particles, further enhancing ionic conductivity [21]. Additionally, lattice strain resulting from pressure-induced dislocations has been reported in Li_6PS_5Br to enhance Li^+ ion transport [22]. Another way of reducing non-conductive voids is the optimization of the particle sizes of the electrode composite components, like those of the solid electrolyte and cathode active materials [23]. Investigation of the densification of Li_6PS_5Cl separator tapes revealed significant influences of the pre-processing of powder particles on the microstructure and emphasizes on the necessity of further refinement of both powder processing and densification techniques [9]. While the effect of pressure on the structural properties of Li_6PS_5Br argyrodite has been investigated, the influence of the particle size on the compaction of argyrodite-type materials remains unexplored.

Motivated by the need to further improve solid electrolyte properties and to gain a more complete understanding of the influences of processing; here, we investigate the impact of pressure on Li_6PS_5Cl with varying particle size distribution (4, 11, 20, and 40 μm). In situ impedance measurements under pressure are performed and Heckel analysis is used to investigate the compaction behavior of Li_6PS_5Cl. X-ray diffraction (in situ and ex situ) in combination with pair distribution function analysis are used to monitor the structural changes upon and after applying pressure. Dark field X-ray microscopy orientation maps further highlight the structural differences on Li_6PS_5Cl agglomerates after the pressure application. Simulations on Li_6PS_5Cl densification show that the inhomogeneity of PSD in Li_6PS_5Cl significantly influences the strain levels experienced by the particles. However, microstructures with homogeneous PSD simulations demonstrate a very consistent stress distribution. The findings of this work highlight the critical role of solid electrolyte design in tailoring microstructural characteristics to achieve overall improved solid-state battery performance.

2 | Results and Discussion

2.1 | Compaction of Li_6PS_5Cl with Varying Particle Sizes

Fabrication and stack pressure [8] applied on solid electrolytes are unavoidable steps for impedance measurements and cycling of solid-state batteries [24]. The application of external, uniaxial pressure (compression) leads to the densification of the loose powder (schematically represented in Figure 1a). During densification, the powder particles are packed more efficiently, particle-particle contact is improved by minimizing the empty space (voids) among them, i.e., impacting the porosity [25]. Higher pressures used for the consolidation of solid electrolytes result in a fully compressed, dense and mechanically stable pellet. The entire process of densification and consolidation is also defined as compaction. Here, a pressure range from 0.1 to 1.5 GPa is used to investigate the densification process of

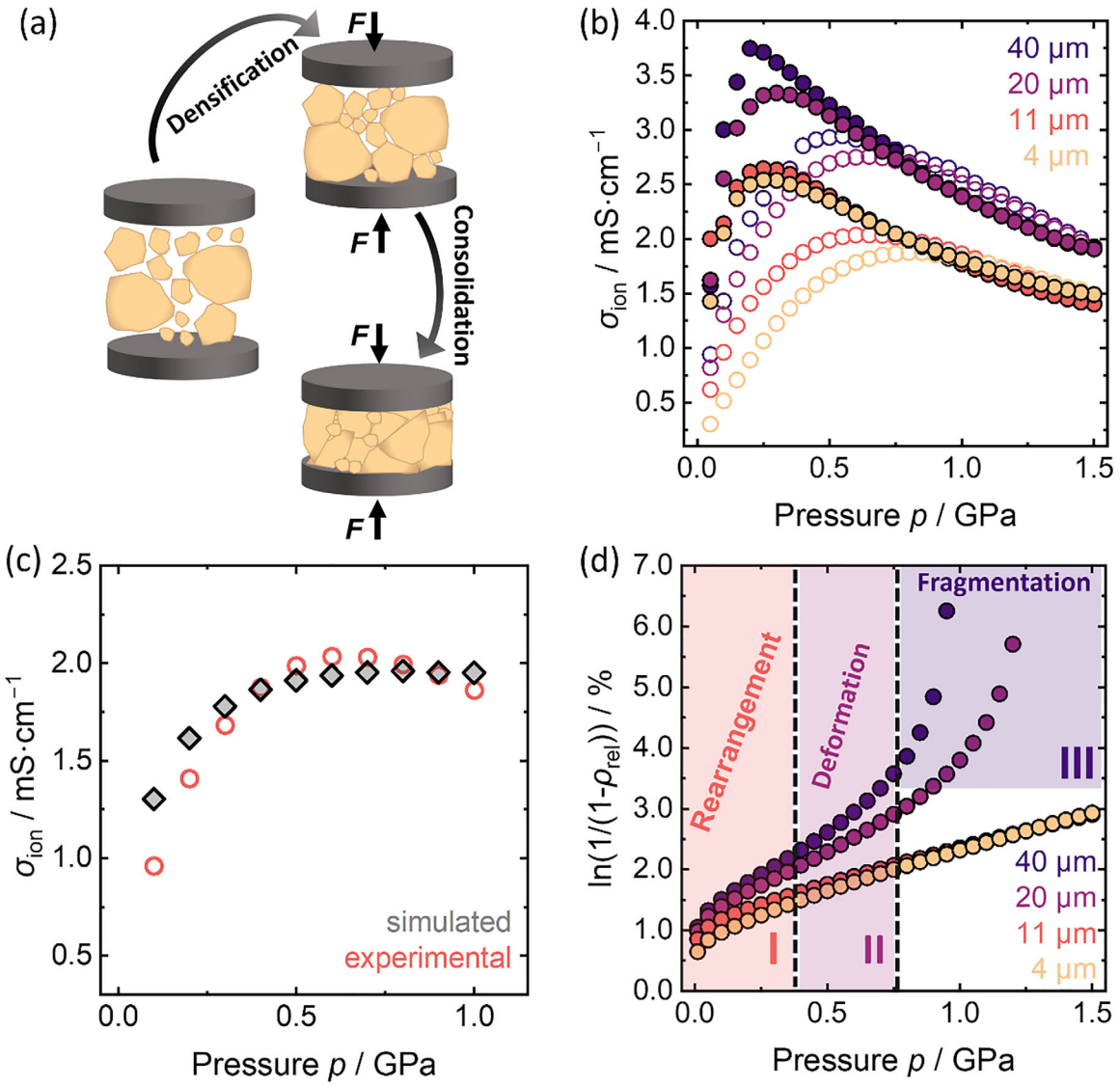

FIGURE 1 | Compaction of Li_6PS_5Cl with varying particle sizes. (a) Schematic representation of the compaction process, including the densification and consolidation of the powdered materials. (b) The influence of pressure on the ionic conductivity. (c) The impact of pressure on the $\sigma_{ion,sim}$ of Li_6PS_5Cl–11 µm of the DEM-simulated microstructure vs. the experimental $\sigma_{ion,exp}$. (d) Heckel analysis is used to investigate the compaction behavior of the Li_6PS_5Cl powders with varying particle sizes under pressure.

Li_6PS_5Cl powders with four different particles size distributions (provided by AMG Lithium and marked by their respective D_{50} values as 4, 11, 20, and 40 µm). The hollow data points represent measurements where the pressure applied on the powdered samples was increasing up to 1.5 GPa (Figure 1b). The filled data points represent measurements where the pressure was decreasing, and thus, the pellets were already densified. For pressures higher than 0.7 GPa, there is the so-called activation volume regime, where a linear behavior of ln(σ) vs. pressure is observed and the unit cell contraction takes place [26, 27].

In terms of ionic conductivity, two distinct groups can be separated from their behavior under pressure (Figure 1b): Li_6PS_5Cl with smaller PSD (4 and 11 µm) and Li_6PS_5Cl with larger PSD (20 and 40 µm). Li_6PS_5Cl with smaller PSDs exhibit a generally/overall slightly lower ionic conductivity, while Li_6PS_5Cl with larger PSDs present a higher conductivity. The distinct regimes of the densification regime, compression and decompression are depicted exemplarily only for Li_6PS_5Cl–11 µm (Figure S1), since the same behavior is observed for all Li_6PS_5Cl in this study and the focus is to emphasize on the different regimes. The calculated ionic conductivity from the DEM-generated microstructures ($\sigma_{ion,sim}$) exhibits a monotonic increase with applied pressure, consistent with progressive densification of the microstructure (Figure 1c). Each microstructure was taken at different points upon compression reaching up to 1.6 GPa. A monotonic increase of ionic conductivity with increasing pressure is observed in the system. The process of microstructure compaction leads to reduced thickness and increased contact points between particles, thus yielding higher ionic conductivity values compared to previous states. It is important to note that the DEM simulations do not account for pressure-induced changes in lattice parameters or variations in intrinsic material properties. As such, the observed enhancement in the calculated ionic conductivity can be attributed only to geometric factors, i.e., particle rearrangement and void reduction. Despite this simplification, the simulation

results align well with the experimental trend, indicating that the primary mechanism driving increased ionic conductivity during compression in this pressure range is the microstructural. The observed difference in the ionic conductivity between the experimental data and simulations stems from the assumed geometrical properties of the microstructures. This assumption impacts the percolation pathways, leading to differences in microstructural voids and particle distribution. However, their differences tend to disappear under high pressure as Li_6PS_5Cl forms an intact, fully connected structure.

The relative density of the densification process is investigated and shows that Li_6PS_5Cl, consisting of larger particles (40 µm), presents 100 % relative density at lower pressure (1 GPa), following the Li_6PS_5Cl–20 µm material with a 100 % densification at 1.2 GPa (Figure S2). However, Li_6PS_5Cl with smaller particles (4 and 11 µm) present a densification of 95 % relative density, even after an applied pressure of 1.5 GPa. Heckel analysis is used to investigate the compaction behavior of Li_6PS_5Cl powders under applied pressure (Figure 1d). The smallest particles reveal a linear and gradual increase, indicating a steadier densification process. While linear regions at low pressures indicate plastic deformation, the largest particles (Li_6PS_5Cl–20 µm and Li_6PS_5Cl–40 µm) present a deviation from linearity at higher pressure. This behavior is attributed to fragmentation [28] or particle fracturing [13]. This may indicate that high pressure leads to cracking of larger particles and the formation of smaller particles [29, 30]. These small particles then serve to fill the voids between the larger ones potentially leading to the full densification behavior at larger PSD.

2.2 | Structural Changes of Li_6PS_5Cl with Varying Particle Sizes

Solid-state NMR spectroscopy is used to investigate the local environments of pristine and pressed samples with varying particle sizes, by recording both ^{6}Li and ^{31}P MAS NMR spectra. In the ^{6}Li MAS NMR spectra, a slight increase in ^{6}Li linewidth is observed for all pressed samples, which can be attributed to increased strain introducing disorder in the local lithium environments (Figures S3 and S4 and Table S1). However, it is important to note that all ^{6}Li linewidths remain below 10 Hz, indicating that the changes in local environments are relatively small. Moreover, no significant changes are observed in the ^{31}P MAS NMR spectra, suggesting that the PS_4^{3-} tetrahedra remain unaffected by the applied pressure (Figures S5 and S6). To evaluate how changes of local structure influence ion transport, static variable-temperature (VT) saturation recovery ^{7}Li experiments were performed. These results show that all unpressed and pressed samples exhibit a single dominant dynamical process in the MHz regime (Figures S7a,b and Table S2). The activation energy (E_a) is found to be the same within experimental uncertainty of the method for all the pressed materials (Figure S7c).

To better understand the influence of pressure on the structural changes of these materials, X-ray diffraction is employed both for the pristine Li_6PS_5Cl (Figure S8a) and for the Li_6PS_5Cl materials after pressing at 1.5 GPa (Figures S9 and S10). The pristine materials crystallize in the $F\bar{4}3m$ space group [31] (Figure S8b). Significant reflection broadening is observed after pressure application, with Li_6PS_5Cl–4 µm exhibiting the largest reflection broadening (Figure 2a). The reflection broadening is attributed to the induction of strain in the form of dislocations due to pressure application and has already been explored in argyrodite materials [22].

To further elucidate the influence of pressure on Li_6PS_5Cl with varying particle sizes, in situ synchrotron high-pressure powder X-ray diffraction is used to investigate the structural changes of Li_6PS_5Cl–4 µm and Li_6PS_5Cl–11 µm (Figure 2b; Figure S11). The reflection shift to higher Q values is related to the unit cell contraction due to the decreasing lattice parameter, a (Table S3). Following, the strain of the pressed Li_6PS_5Cl with varying PSD is quantified via Williamson-Hall analysis, as well as by Rietveld refinements and the Stephens strain model (Figure 2c) using the ex situ X-ray diffraction data. Li_6PS_5Cl–4 µm exhibits the highest amount of strain, while comparable lattice strain is observed in the other samples. Next, the strain extracted from in situ synchrotron high-pressure powder X-ray diffraction is calculated for the Li_6PS_5Cl–4 µm and Li_6PS_5Cl–11 µm materials (Figure S12). The Williamson-Hall analysis for the in situ synchrotron high-pressure powder X-ray diffraction data reveals a lower strain induced in Li_6PS_5Cl–4 µm (strain = 0.81(4) %) compared to Li_6PS_5Cl–11 µm (strain = 1.27(6) %) (Figure S12). This can be attributed to the limited number of particles probed during the high-pressure powder X-ray diffraction experiment, in contrast to the ex situ X-ray diffraction analysis, which reflects a bulk average. Thus, the measurement does not represent a good average of the bulk behavior, especially considering the size of the single particles in the sample and the beam size of approximately 60 µm. The strain contour plots and the evolution of the strain, with a preferred strain-direction according to Stephens of [110], is presented in Figure S13, and all strain values can be found in Table S4. Although this finding suggests a difference in the strain induced by pressure between a finite number of particles (in situ) and the bulk material (ex situ); the reason for this difference is at this point unclear. However, we will investigate this observation in greater detail in the following parts of this work.

Long-range pair distribution function analysis in the range from 0.8 Å to 80 Å for the pristine and pressed materials (Figures S14a,c) shows a significant decrease of the coherence length in the pressed materials (Figure 2d). On the short-range scale from 1.5 Å to 20 Å, on the other hand, no significant difference can be observed (Figures S14b,d). Although the bulk Li_6PS_5Cl–4 µm material presents the highest strain of all different PSDs, it is yet unclear why pressure has the highest impact on this material. The strain can be visualized by the strain contour plots (Figure 2e), which show how the strain distribution varies in a 3D region. The higher amount of strain is observed for Li_6PS_5Cl–4 µm, while the other three materials present similar anisotropic strain distribution.

2.3 | Diffraction Imaging Measurements and Intragranular Orientation Variations within a Single Li_6PS_5Cl Particle

To further investigate the dislocations induced in these materials by pressure, dark field X-ray microscopy is used. Although the hypothesis of dislocations in the Li_6PS_5Br argyrodite structure has

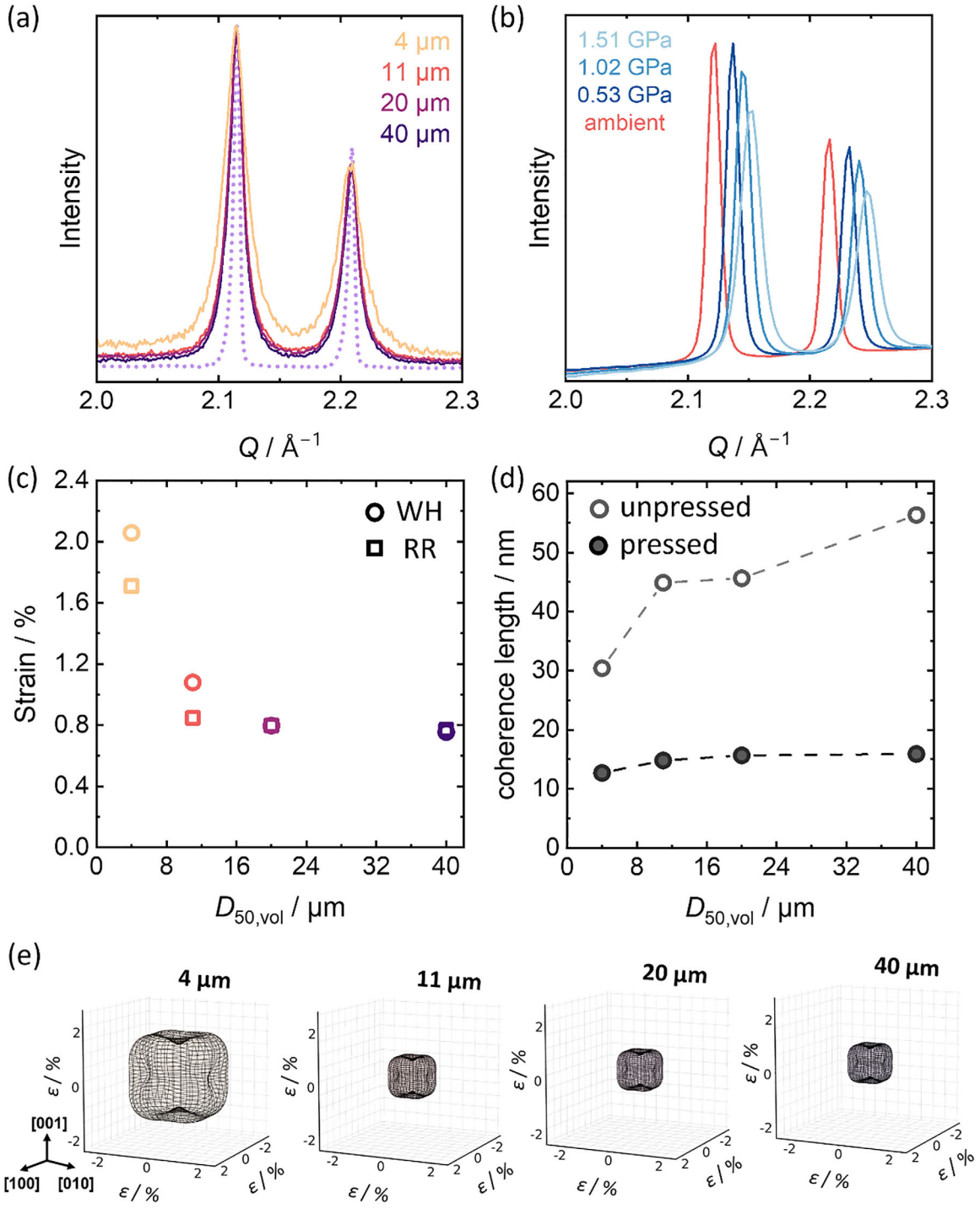

FIGURE 2 | How particle size affects strain in Li_6PS_5Cl. (a) X-ray diffraction reveals reflection broadening in the pressed materials. The dotted pattern corresponds to the unpressed Li_6PS_5Cl–11 µm and is used as a reference to better visualize the difference in the reflection broadening between strained and unstrained materials. (b) Synchrotron high-pressure powder X-ray diffraction shows the contraction of the unit cell by shifting to higher Q values. (c) Strain extracted by two different methods; Williamson Hall (WH) and via Rietveld refinements (RR) using ex situ X-ray diffraction data. (d) The coherence length as extracted from pair distribution function analysis using an envelope function. (e) The strain contour plots for the materials after 1.5 GPa, showing anisotropic strain distribution. The higher amount of strain is observed for Li_6PS_5Cl-4 µm.

already been presented and analysed (Figure 3a) [22], there has been no direct experimental observation of dislocations shown so far. Here, by using DFXM measurements [32] (Figure 3b), we aim to investigate the local orientation and strain of single particles (Figure 3c). DFXM does not resolve individual dislocation cores unless the dislocation spacing is above the spatial resolution of the system [33], which is typically not the case in these types of materials. However, in this study, we measure the misorientation within grains by mapping the intragranular orientation spread, which arises from underlying dislocation structures. When the dislocation spacing becomes smaller than the resolution limit (set by the diffraction-limited imaging system and detector pixel size),

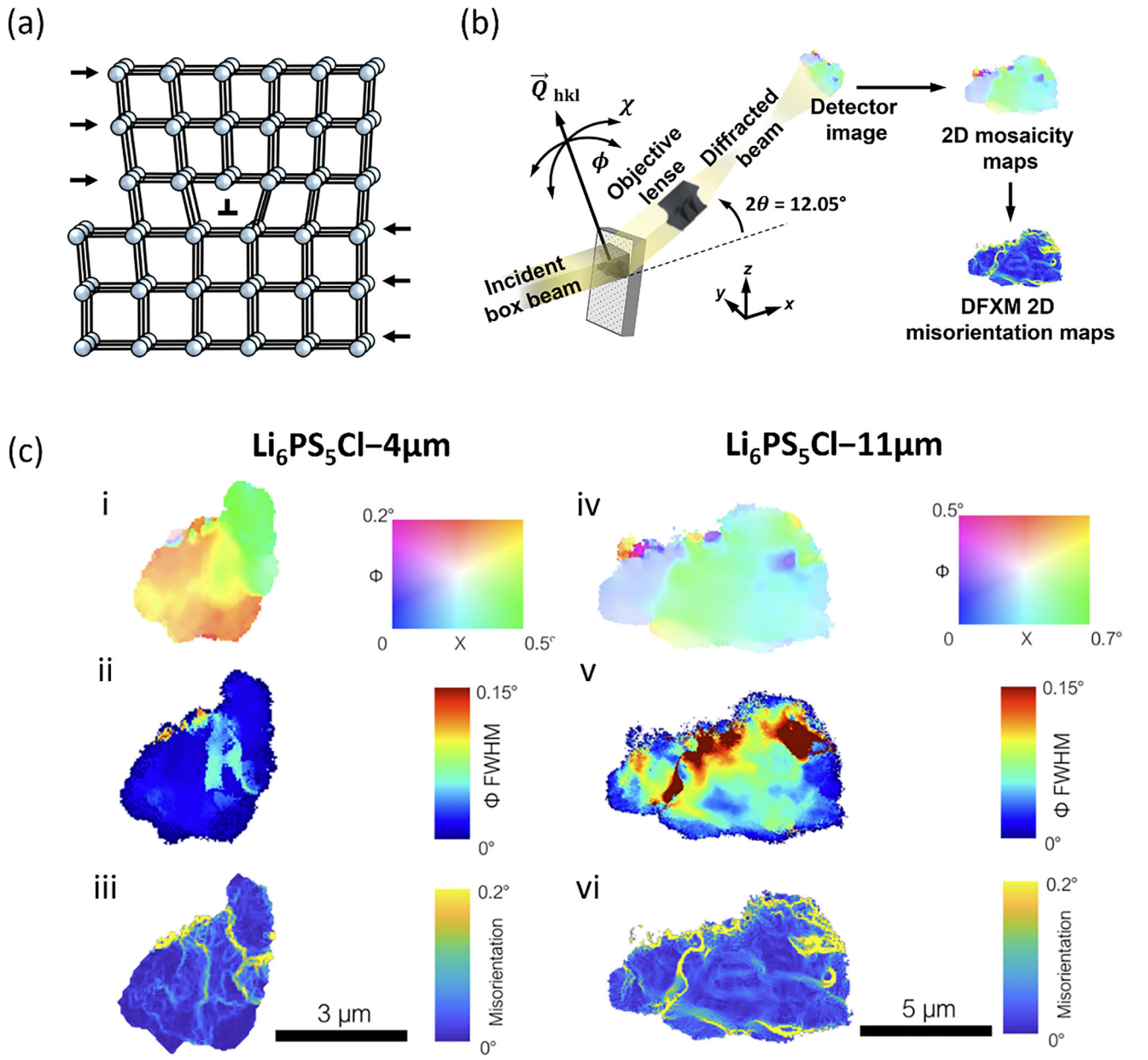

FIGURE 3 | Diffraction imaging measurements. (a) Schematic representation of a dislocation core in a cubic lattice. (b) Schematic representation of the DFXM set-up. (c) DFXM orientation maps of Li_6PS_5Cl–4 μm (i, ii, iii) and LiPSCl–11 μm (iv, v, vi) illustrate the local orientation variations around the hkl diffraction vector. Panels (i) and (iv) depict mosaicity maps, which combine the center-of-mass (COM) information from both the φ and χ tilts. Panels (ii) and (v) display the full-width at half maximum (FWHM) of the φ distribution across the grains, serving as a proxy for dislocation density through the relationship FWHM $\sim \sqrt{\rho}$GND. Lastly, panels (iii) and (vi) present maps calculated from the spatial gradients of the COM maps, quantifying the intragranular misorientation as $\sqrt{(\Delta\varphi^2 + \Delta\chi^2)}$. These maps provide a comprehensive view of the orientation and strain distributions, highlighting the microstructural differences between the two samples.

it is no longer possible to see isolated dislocations but the lattice curvature or misorientation fields caused by their presence is still detectable.

The mean misorientation for a Li_6PS_5Cl–4 μm particle is 0.0394 whereas this number is 0.0727 for a single analysed Li_6PS_5Cl–11 μm agglomerate. For the sample with a mean misorientation of $\Delta\theta = 0.0394°$, the calculated GND density is approximately ρGND $\approx 1.14 \times 10^{12}$ dislocations/m^2. This value is consistent with the distribution observed in the misorientation histogram (Figure S15), which shows a notable population of higher misorientation angles across the grain boundaries.

Such misorientation variations indicate a significant degree of local lattice distortion, further supporting the presence of a larger dislocation density. The correlation between the histogram data and the calculated GND density underscores the sensitivity of the microstructure to strain accommodation mechanisms within the grain. This higher density of dislocations suggests increased plastic activity, likely influenced by the crystal's deformation history or intrinsic defects. These findings highlight the

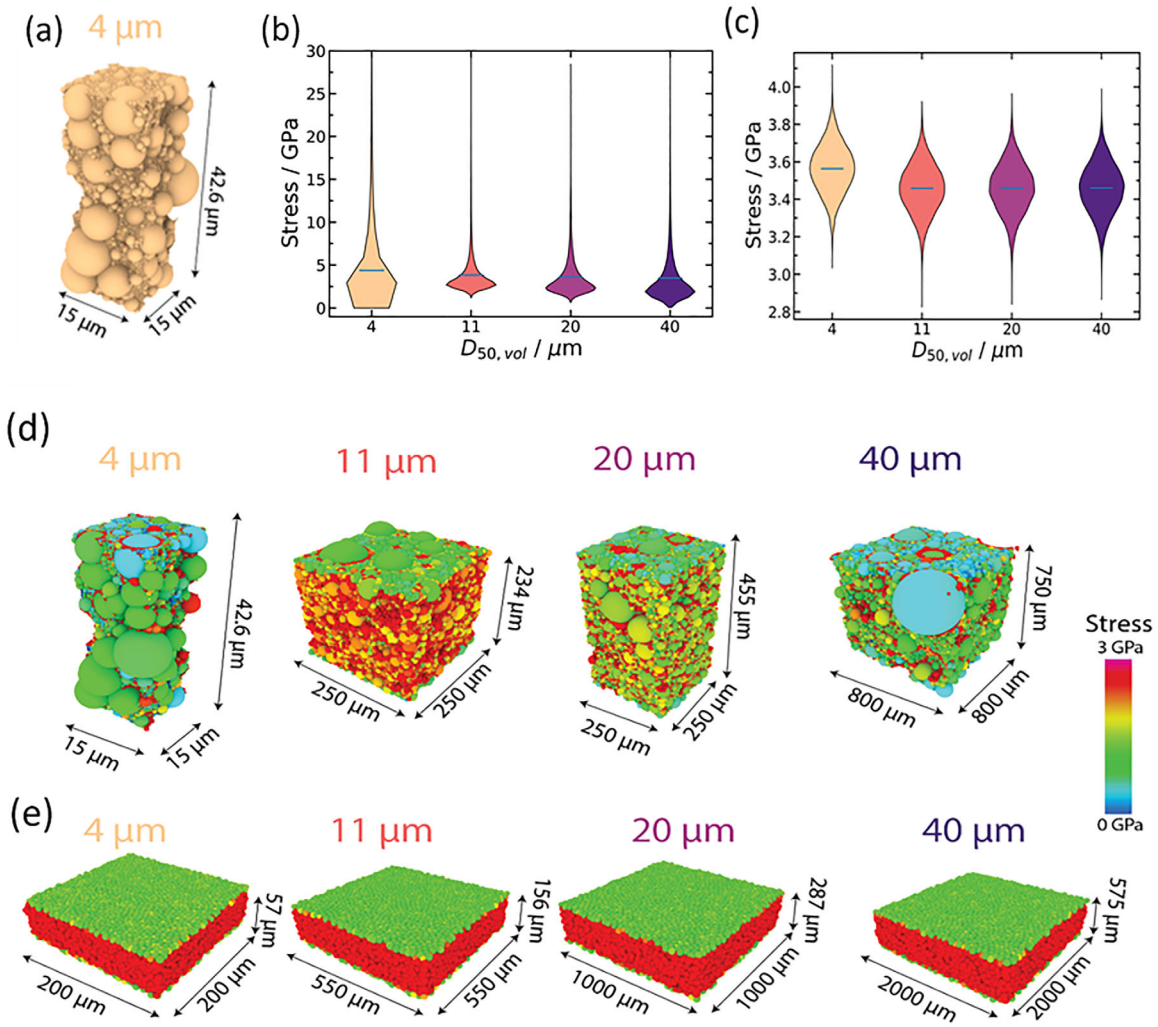

FIGURE 4 | DEM Simulations. (a) DEM-simulated Li_6PS_5Cl microstructures composed of experimentally measured PSD for Li_6PS_5Cl–4 µm. (b,c) Violin plots illustrating the simulated distribution of particle-level stress, based on D_{50} for compressed structures composed of (b) experimentally measured PSD and (c) single particle size. (d,e) Simulated stress-resolved Li_6PS_5Cl microstructures visualized with particles color-coded according to the local stress exerted on the particle along z axis for (d) experimentally measured PSD and (e) single particle size.

importance of the local microstructure when looking at the pressure introduction of strain in these materials. These results present the first demonstration of DFXM applied to powder-like diffraction patterns from particles. In contrast to bulk crystals, such as polycrystalline grains, single crystals or thin films; this work presents the imaging of orientation fields in discrete particles in the micron-scale, which is a significant methodological advancement. Here, resolving intragranular orientation variations within a single Li_6PS_5Cl particle, with spatial and angular resolution sufficient to detect strain and dislocation structures was achieved.

2.4 | Impact of Particle Size Distribution on Stress Heterogeneity

To gain a deeper understanding of the mechanisms underlying the compaction behavior of Li_6PS_5Cl, DEM simulations were conducted using varying PSDs. The experimental PSDs and scanning electron microscopy (SEM) images of the different Li_6PS_5Cl powdered material are provided (Figures S16 and S17). Simulated microstructures (Figure 4a; Figure S18a) employing the experimentally measured PSD exhibit pronounced fluctuations in stress along the z-coordinate, with smaller particles experiencing significantly higher stress levels (Figure 4b; Figures S19 and S20). In the analysis of the DEM simulation results, the outermost 20 % regions at both the top and bottom regions of the microstructure were excluded in Figure 4b,c to eliminate boundary effects arising from particle–wall interactions. This approach ensures that the evaluation reflects the intrinsic response of the bulk material to compression. In contrast, simulated microstructures composed of a single particle size (Figure S18b) display a very homogeneous stress distribution, both spatially and across all particles (Figures S19b,d). In these single particle size systems, stress magnitudes appear largely independent of the particle size, indicating uniform mechanical loading across the microstructure (Figure 4c; Figure S19b).

To ensure the fidelity and direct relevance of the DEM analysis (Figure 4) to the experimental observations, the PSDs used for all simulations were identical to those measured experimentally for each respective Li_6PS_5Cl sample (Figure S16). Consequently,

the modeled systems, such as the Li_6PS_5Cl–4 μm sample, accurately reflect the inherent polydispersity of the physical powders, comprising a mixture of particle sizes rather than a simple monodisperse collection. This direct correspondence ensures that the DEM results, particularly those relating to stress distribution and strain, are grounded in the actual microstructure and heterogeneity of the materials investigated in Figure S17.

The calculations demonstrate that the spread of particle sizes within the PSD exerts a significant influence on stress heterogeneity, rather than the PSD itself. Inhomogeneous PSDs result in more pronounced stress variations, driven by non-uniform particle-particle interactions and resulting in an uneven stress distribution (Figure 4b; Figure S20). This inhomogeneity leads to elevated stress concentrations in smaller particles, which may enhance their susceptibility to plastic deformation and dislocation activity. However, when the microstructures are composed of single particle sizes, the stress distribution remains consistent, leading to the conclusion that the broad particle size distribution of Li_6PS_5Cl–4 μm is the reason for the increased experimentally observed strain in this material. Figure 4d depicts the simulated microstructures composed of the experimental PSD of Li_6PS_5Cl, and Figure 4e shows the simulated microstructures of the single size particle systems. All particles in the simulated microstructures are color coded based on the stress magnitude applied in the *z*-coordinate, which ranges from 0 to 3 GPa. The particles within the microstructures with experimental PSD are exposed to a high variation of stress due to their sizes, where stress higher than 3 GPa is exerted on small particles, and larger particles are experiencing lower stress. In Figure 4e, it is noticeable that particles closer to the walls experience lower stress due to particle-wall interaction. However, the stress applied to interior particles of the microstructures is homogeneous and mostly around 3.5 GPa (Figure 4c). The observation that different, single-size particle distributions exhibit similar stresses is a general effect in contact mechanics and largely independent of the materials class. In polydisperse packings, smaller particles tend to exhibit higher contact pressure and stress, especially under uniaxial compaction. This results from Hertzian contact mechanics, sample geometry, where small particles are confined in tight pores and thus increase the sampled contacts per unit volume [34].

To further evaluate the importance of the broad particle size distribution of Li_6PS_5Cl, sieving of Li_6PS_5Cl–4 μm is investigated here (Figure 5a). The pressure-induced strain calculated from the Williamson-Hall analysis is significantly decreased when Li_6PS_5Cl–4 μm presents a more homogeneous particle size distribution (Figure 5b), further confirming the high-pressure synchrotron diffraction measurements and the DEM simulations. Additionally, the compaction behavior of a mixture consisting of Li_6PS_5Cl–40 μm and Li_6PS_5Cl–4 μm particles is also examined. Here, the question is if we can control the fragmentation observed above in the larger particles. To target this, a mix of Li_6PS_5Cl with 40 and 4 μm particles is prepared, with the hypothesis that filling of the voids existing in the Li_6PS_5Cl–40 μm pellet will prevent the fragmentation of the larger particles (Figure 5c). Heckel analysis reveals that the area of fragmentation is no more visible for the mixture of 40 and 4 μm particles, further confirming our hypothesis. This emphasizes the importance of considering not only the absolute particle size when choosing solid electrolytes, but also the distribution of the particle sizes.

This is particularly important for their use in solid-state batteries since solid electrolytes for the single elements (anode, cathode and separator) may require different size distributions. Broad particle size distributions optimized for high density may be advantageous in separator layers, allowing thinner layers and thus higher energy densities [35]. Narrow distribution on the other hand—tailored to create specific porosity in the cathode and anode layers—may enhance cycling stability, by providing controlled porosity to counteract contact losses due to volume changes during cycling, particularly important in the development of conversion type electrode composites [36–38].

3 | Conclusion

This work explores the impact of pressure on the densification of Li_6PS_5Cl across different particle size distributions (4, 11, 20, and 40 μm). In situ impedance measurements track changes under pressure, while Heckel analysis is employed to characterize the compaction behavior of the powders. Smaller particles exhibit steady densification, whereas larger particles undergo fragmentation during compaction. Structural changes induced by pressure are investigated using X-ray diffraction, revealing higher strain in smaller particles, and pair distribution function analysis shows reduced coherence length in the pressed samples. Dark-field X-ray microscopy orientation maps further highlight intragranular differences within Li_6PS_5Cl agglomerates, particularly the higher misorientation and inferred dislocation density in an 11 μm particle compared to a 4 μm particle.

Discrete element method simulations provide additional insight into the origins of strain. The results show that strain levels are strongly influenced by particle size distribution (PSD) inhomogeneity rather than absolute particle size. Systems with smaller particles and broader PSDs experience higher stresses, while homogeneous PSDs exhibit consistent stress distributions regardless of particle size. Complementary experimental results support these findings: sieving smaller particles to narrow the PSD reduces lattice strain, confirming that homogeneity in particle size distribution mitigates strain development during densification.

Both the simulation and the experiments capture the impact of the initial regime where the conductivity rises with increasing pressure due to geometric densification, on conductivity, where increasing pressure enhances particle–particle contact and thereby increases ionic pathway connectivity across all PSDs; however, the experiments reveal an additional microstructural degradation regime, absent in DEM due to its limited spatial resolution, where fragmentation, increased grain interfaces, and microstrain accumulation in systems with smaller particles or broad PSDs begin to counteract the geometric compaction effect. This transition occurs once densification forces promote intragranular deformation rather than merely rearrangement, leading to disrupted transport-path continuity and ultimately lower overall conductivity in fine or highly heterogeneous PSDs.

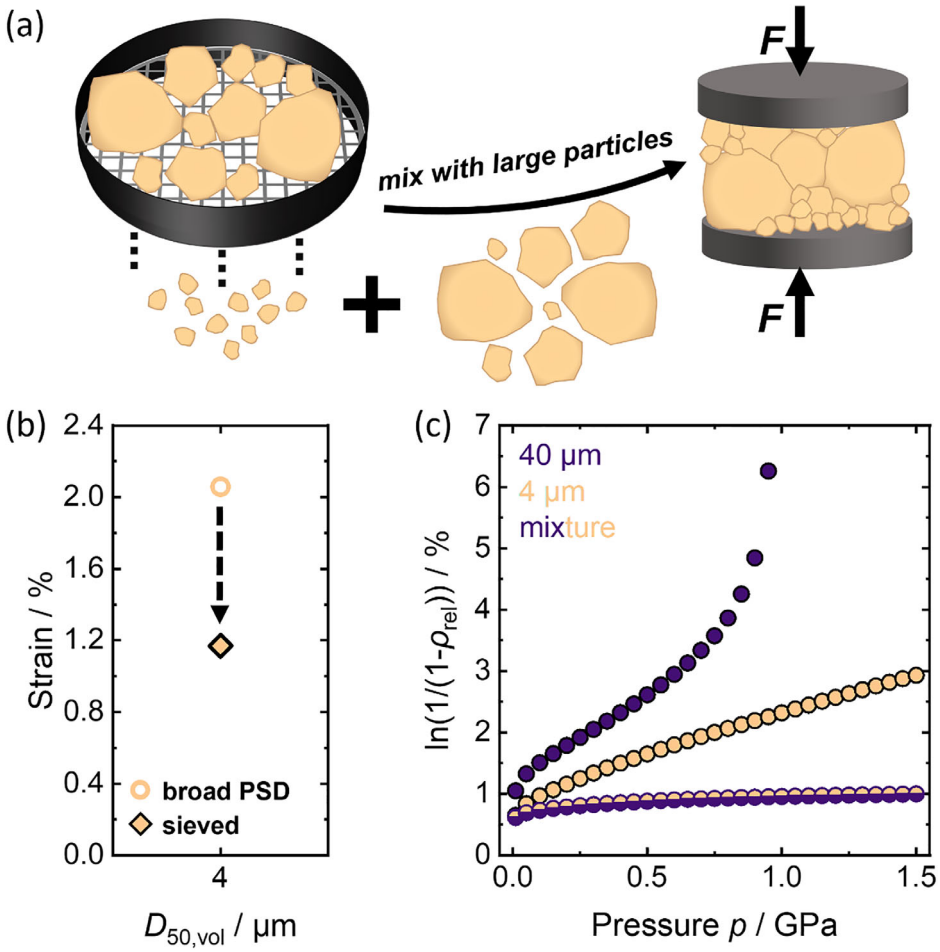

FIGURE 5 | Tuning of particle size distribution for better compaction of Li_6PS_5Cl. Graphical representation of Li_6PS_5Cl−4 µm sieving to investigate the impact of homogeneity in the strain after applied pressure. Further mixing of the sieved Li_6PS_5Cl−4 µm with Li_6PS_5Cl−40 µm to investigate the fragmentation of larger particles when the voids are filled. (b) Sieving of non-homogeneous Li_6PS_5Cl−4 µm results in a material with decreased amount of strain after pressure application, confirming that the inhomogeneous particle size distribution was the cause for the high strain in this material. The open circle corresponds to LPSCl−4 µm with a broad PSD, while the filled rectangle corresponds to LPSCl−4 µm with a narrow PSD. (c) The mixture of 40 and 4 µm Li_6PS_5Cl shows a linear increase, revealing that the fragmentation can be prevented when filling the voids with smaller particles.

Based on these findings, different considerations need to be taken into account when choosing both the particle size and the particle size distribution of Li_6PS_5Cl solid electrolytes as solid state battery components. For separator layers, maximizing density and mechanical integrity is crucial to suppress Li^+ dendrite penetration and to minimize the volume fraction of the solid electrolyte within the solid-state battery. Thus, narrow, homogeneous PSDs are preferable for separators, as local stress concentrations are minimized, mitigating fracturing and promoting uniform load distribution. Moreover, a combination of large and small particles of narrow PSDs can achieve high densifications at moderate pressure while limiting particle stress, thus ensuring structural stability of the separator layer. For electrode components on the other hand, broad, inhomogeneous PSDs of small particle sizes may be preferable. They allow controlled voids within electrode composites, counteracting volume changes during cycling, as well as providing optimized particle contact between solid electrolyte and active material due to large surface areas and contact. Additionally, the increased local strain and particle rearrangement associated with wide PSDs, along with fragmentation and intergranular misorientation, may create additional ion-transport pathways, which is often the limiting factor for cyclability in solid-state batteries.

Overall, these results demonstrate that the compaction behavior of solid electrolytes is governed not simply by particle size, but by the inhomogeneity of the size distribution. This work bridges micro- and macro-scale observations, underscoring that the microstructural composition of solid electrolytes plays a critical role in structural evolution under pressure and, ultimately, in determining the performance of solid-state batteries.

4 | Experimental Section

4.1 | Uniaxial Applied Pressure Experiments for Strain Introduction and Potentiostatic Electrochemical Impedance Spectroscopy (PEIS)

A CompreDrive setup (rhd instruments) was used for the pressure-dependent experiments. 100 mg of Li_6PS_5Cl was loaded into a 6C CompreCell (6 mm diameter) under Ar atmosphere

(H_2O <0.5 ppm and O_2 <0.5 ppm). Pressure was applied uniaxially and kept constant with high accuracy (0.5%) and the piston movement was monitored during the entire measurement. An external heating mantle kept the internal temperature of CompreCell constant at $T = 298$ K, controlled via a Presto A40 thermostat (Julabo). AC impedance spectroscopy was utilized to determine the ionic conductivities, and the impedance spectra were recorded with an SP-150 impedance analyzer (Bio-Logic Science Instruments Ltd.) at room temperature. The temperature was equilibrated at $T = 298$ K for two hours, at the beginning of each measurement, to ensure complete stabilization of the pellet temperature. Potentiostatic electrochemical impedance spectroscopy (PEIS) was recorded utilizing a sinusoidal excitation voltage signal of 150 mV in a frequency range from 1 MHz to 100 mHz. The resulting impedance spectra were evaluated with RelaxIS 3 Impedance Spectrum Analysis software (rhd instruments), and the data quality was examined by using the Kramers-Kronig relations to determine the reliable frequency range for data fitting. All measurements were carried out as triplicates with statistical standard deviation values smaller than the plotted size of the data points.

4.2 | Heckel Analysis

Heckel analysis was a technique used to characterize the compaction behavior of powders under applied pressure. By relating the applied pressure to the relative density of the pellet, it provided insights into deformation mechanisms and mechanical properties, i.e., plasticity and yield pressure of materials. There were two types of Heckel analysis. The "in-die" (at pressure) accounts for powder deformation upon applying pressure—in compression. The "out-of-die" (zero pressure) analysis could be used in an already compacted material and also accounts for its elastic recovery. The Heckel equation [39] (Equation 1) is derived from first-order kinetics and describes the relationship between applied pressure and relative density,

$$\ln\left(\frac{1}{1-\rho_{rel}}\right) = Kp + A \tag{1}$$

where ρ_{rel} is the relative density of the pellet, which is equal to the experimental density divided by the crystallographic density for every pressure measurement. K and A are the slope and intercept of the linear region of the Heckel plot. The experimental densities were determined by monitoring in situ the motor movement of the CompreDrive setup (rhd instruments) and then calculating the piston movement. The crystallographic densities of the different Li_6PS_5Cl materials were extracted from Rietveld refinement results of the pressed materials after compaction.

4.3 | Ex Situ Powder X-Ray Diffraction

Powder X-ray diffraction measurements were performed on a laboratory STOE STADI P diffractometer in Debye-Scherrer geometry with a Dectris MYTHEN2 1K detector in Debye-Scherrer mode at room temperature. The radiation source was Cu $K_{\alpha 1}$ ($\lambda = 1.5406$ Å) employing a Ge(111) monochromator. The X-ray diffraction data was collected within a 2θ range from 10° to 90° in 0.015° steps. To avoid material degradation in air, all samples were measured in sealed borosilicate glass capillaries with a diameter of 0.5 mm to ensure no reaction with air and moisture.

4.4 | In Situ Synchrotron High-Pressure Powder X-Ray Diffraction

Synchrotron high-pressure powder X-ray diffraction was performed using diamond anvil cells (DACs) at the I15 beamline, at Diamond Light Source, UK. The wavelength used was $\lambda = 0.31$ Å, and a 2D CdTe Pilatus3 2M area detector was used for data collection. LaB_6 was used as a calibration standard to determine the detector distance. Integration of 2D diffraction images was performed using the DIOPTAS software [40], while Rietveld refinements were performed using the TOPAS-Academic V7.25 software package [41]. Silicone oil was selected as the pressure-transmitting medium, which can be expected to maintain hydrostatic conditions during compression within the measured pressure range [42]. In this way, the isotropic application of pressure in the whole area of the sample could be achieved [43]. The gasket material was 200 µm foil of steel, preindented to a thickness of 80–100 µm and with a 400 µm diameter hole EDM 'drilled' into it to form the sample chamber. Samples, ruby and silicone oil, were loaded into the DAC under Ar inert atmosphere. Loaded samples were freely floating in the pressure medium and not bridging the anvils. The applied pressure was in a range from ambient to 1.5 GPa in $\Delta p = 0.1$ GPa steps. The pressure was adjusted using a LeToullec style membrane-type DAC with 700-micron culets, and the pressure was determined by the Ruby luminescence method [44, 45].

4.5 | Williamson-Hall Analysis

The Williamson Hall analysis was carried out as described elsewhere [22]. According to the Williamson-Hall method [46], diffraction line broadening could be attributed to the presence of internal strain and grain size contributions, which had different functional dependencies on scattering angle, i.e., 2θ. The degree of peak broadening, quantified by the full width at half maximum (FWHM) or, more generally, the integral breadth (β) of the diffraction peaks, which could be extracted from X-ray diffraction data and used in the Williamson-Hall equation,

$$\beta\cos(\theta) = (C\varepsilon_{\mathrm{XRD}})\ \sin(\theta) + \frac{\lambda}{d_{\mathrm{XRD}}} \tag{2}$$

This predicted a linear dependence of the quantity $\beta\cos(\theta)$ when plotted vs. $\sin(\theta)$ with the slope being a metric of the internal strain $\varepsilon_{\mathrm{WH}} = C\varepsilon_{\mathrm{XRD}}$, where C was a proportionality factor of the internal strain $\varepsilon_{\mathrm{XRD}}$ and the y-intercept could be related to the grain size, d_{XRD}.

4.6 | Rietveld Analysis and Stephens Anisotropic Microstrain Model Analysis

Rietveld refinements were performed using the TOPAS-Academic V7.25 software package [41]. The structural information of Li_6PS_5Cl, taken from Kraft et al. [47], was

used as a starting model for this study. The peak shape was fitted by refining a LaB_6 NIST standard dataset with a modified Thomson–Cox–Hasting function, a pseudo-Voigt function to obtain and fix the instrumental broadening defined by U, V, X, Y and Z [48]. These parameters were fixed for the subsequent steps. Fit indicators R_{wp}, R_{exp}, and goodness-of-fit were used to assess the quality of the refined structural model. Refinement of fitted parameters was carried out in the given order: (1) scale factor, (2) background fit by a Chebyshev polynomial with nine parameters, (3) zero error, (4) lattice parameter, and (5) the peak shape parameter W—as the only parameter to not be impacted by lattice strain [49]. Upon achieving a suitable profile fit, the (6) atomic displacement parameters, (7) fractional atomic coordinates, and (8) occupancies were refined for all elements except for lithium. The stability of the refinements was ensured by allowing all the parameters to be refined simultaneously over multiple cycles (using randomized starting points while applying a simplified structural model with constraints in agreement with other reports in literature). Based on the refined structural models, the Stephens anisotropic strain model was used to quantify the internal strain, since significant anisotropic peak broadening was observed in the compacted samples. The model allows for refining (9) two independent strain parameters in a cubic system, $S400$, and $S220$, corresponding to the axis direction and surface diagonals of the cubic unit cell of Li_6PS_5Cl [50]. When "cubic equality" $S_{400} = 2S_{220}$ is not observed, the strain in the respective material can be considered to be anisotropic. The resulting values were plotted following the generalized microstrain approach from GSAS II as strain-surface plots [51]. The strain values as calculated by the Stephens anisotropic model were found in Table S3.

4.7 | Pair Distribution Function Analysis

Total scattering data was collected using a Stoe STADI P diffractometer (Ag $K_{\alpha 1}$ radiation: $\lambda = 0.55941$ Å, Ge 111 monochromator) in Debye-Scherrer geometry with four Dectris MYTHEN2 1K detectors. The samples were measured in sealed borosilicate glass capillaries (Hilgenberg) with a diameter of 0.5 mm over a Q-range from 0.8 $Å^{-1}$ to 80 $Å^{-1}$. Data reduction was carried out using PDFgetX3 [52] with a Q-range cutoff of $Q_{max} = 15$ $Å^{-1}$. Small box modeling was performed using TOPAS-Academic V7.25 software package [41]. For the local structure, the data were fitted over an r-range from 1.5 Å to 20 Å where, (1) scale factor, (2) correlated motion factor, (3) lattice parameters, (4) atomic positions and (5) isotropic atomic displacement parameters were subsequently refined. The decay of the intensity toward higher r gives information about the coherence length, which refers to the size of ordered domains within a material. Coherence length values were extracted using a spherical particle model over an r-range from 1.5 Å to 20 Å [53]. Changes in coherence length correspond to changes in particle sizes as well as defects (e.g., strain).

4.8 | Nuclear Magnetic Resonance (NMR) Spectroscopy

Single-pulse ^{6}Li and ^{31}P magic-angle spinning (MAS) NMR experiments were performed on a Bruker DSX 500 spectrometer equipped with a wide-bore superconducting magnet operating at 500.39 MHz (11.75 T) using a broadband 2.5 mm HXY MAS NMR probe (Bruker). The powder samples were packed inside zirconia rotors with a 2.5 mm outer diameter under an Ar atmosphere, and a MAS frequency of 25.0 kHz was used. Pulse lengths of 10 µs (^{6}Li) and 5 µs (^{31}P) for the $\frac{\pi}{2}$ flip angle was used. Recycle delays of 120 and 600 s were used for ^{6}Li and ^{31}P, respectively. All MAS NMR experiments were referenced to ^{6}Li-enriched Li_2CO_3 (0 ppm, ^{6}Li) and 1 M H_3PO_4 (0 ppm, ^{31}P).

Static variable-temperature (VT) saturation-recovery ^{7}Li NMR experiments were performed on a Bruker DSX spectrometer equipped with a wide-bore magnet operating at 200.19 MHz (4.70 T) using a static 5.0 mm HX broadband NMR probe (Bruker). Samples were packed inside zirconia rotors with a 4.0 mm outer diameter. All experiments were conducted at a resonance frequency of 77.78 MHz (^{7}Li) with a pulse length of 4 µs for a $\frac{\pi}{2}$ flip angle. The temperature of the sample was regulated by using a nitrogen gas flow and electrical heating in the temperature range between 220 and 400 K. All recorded solid-state NMR spectra were processed using the TopSpin software package.

4.9 | Discrete Element Method (DEM) Simulations

DEM was used to generate and compress a Li_6PS_5Cl microstructure of 20 000 particles at randomly selected locations. The simulations were conducted within the microcanonical (NVE) ensemble at a constant temperature of 300 K, ensuring conservation of the number of particles, total system energy, and simulation volume. The primary objective of the simulation was to produce a stress-resolved 3D microstructure of compressed Li_6PS_5Cl by numerically integrating Newton's equations of motion.

During the compression phase, periodic boundary conditions were imposed along the lateral directions (x and y), while fixed boundaries were maintained along the compression axis (z-direction), where two rigid walls were implemented. Compression was applied by displacing the upper boundary plane along the z-direction, exerting a gradually increasing force until the pressure on the lateral cross-sectional area reached 1.6 GPa. The lower boundary plane remained stationary, serving as a mechanical support. The simulation progressed until the system approached a converged state, as indicated by the stabilization of key metrics, including the displacement of the loading plane, the force transmitted to the system, and the particle arrangements. Based on the results of preliminary convergence efforts, a simulation time of 8000 µs (8 ms) was decided to be sufficient, as longer durations did not yield significant differences in the results.

Material specific parameters, including the Young's modulus, Poisson's ratio and other coefficients for Li_6PS_5Cl were retrieved from Alabdali et al. [19]. and implemented as part of the Granular Force Fields (GFF) of our DEM approach. The respective values could be found Table S5. All simulations were executed using

the LIGGGHTS software package [54] on a single computational node of the MatriCS platform at Université de Picardie Jules Verne. The node configuration included 375 GB of RAM and 1 processor (Intel Xeon Gold 6148 CPU @ 2.40 GHz, 40 cores).

A GFF was grounded in the premise that when two discrete particles came into contact, the resulting surface deformation could be described by a nonlinear elastic response. This interaction was governed by the Hertzian contact theory, wherein the force required to compress the particles was modulated by an effective stiffness parameter known as the Hertzian modulus. GFFs had proven particularly effective in capturing the mechanical behavior of granular systems under conditions of high strain rates and substantial particle deformation [55].

The total contact force F between two interacting particles was expressed as

$$F = \left(k_n \delta_{ij}^n - \gamma_n v_{ij}^n\right) + \left(k_t \delta_{ij}^t - \gamma_t v_{ij}^t\right) \tag{3}$$

where k_n and k_t represented the normal and tangential elastic constants, respectively. The terms δ_{ij}^n and δ_{ij}^t denoted the overlap distance in the normal direction and the tangential displacement vector between two contacting spherical particles i and j. The damping coefficients γ_n and γ_t corresponded to the viscoelastic dissipation in the normal and tangential directions, respectively. The quantities v_{ij}^n and v_{ij}^t represented the normal and tangential components of the relative velocity within the particle pair.

4.10 | Ionic Conductivity Calculations

To evaluate the evolution of ionic transport properties under mechanical compression, the GeoDict software suite [56] was employed to analyze the compressed Li_6PS_5Cl–11 µm microstructures obtained by the DEM simulations. The simulated ionic conductivity ($\sigma_{ion,sim}$) was attributed to the continuous percolating network of Li_6PS_5Cl particles offering Li-ion transport capabilities. $\sigma_{ion,sim}$ serve as quantitative descriptor for assessing the influence of the compression protocol on the ionic pathways of Li_6PS_5Cl.

The $\sigma_{ion,sim}$ was calculated using the relation

$$\sigma_{ion,sim} = \sigma_{bulk} \times \left(\frac{D_{ion}}{D_{bulk}}\right) \tag{4}$$

where σ_{bulk} was the intrinsic bulk ionic conductivity of Li_6PS_5Cl equal to 2.0 mS·cm^{-1} (in accordance to the experimentally determined room-temperature ionic conductivity) and D_{ion} and D_{bulk} were the effective and bulk diffusion coefficients for Li^+, respectively. The ratio D_{ion}/D_{bulk} was obtained by numerically solving the Fick's first law within the ion-conductive phase, assuming a concentration gradient Δc imposed across the outer xy planes of the analyzed microstructure.

The effective diffusivity D_{ion} was determined from the net ionic flux, j, according to the following equation

$$D_{ion} = -\frac{j \cdot L}{\Delta c} \tag{5}$$

where L denoted the length of the structure along the transport direction. Periodic boundary conditions were applied in the lateral xy dimensions to mimic the continuous nature of the conductive medium. This methodology enabled the assessment of how the microstructural evolution under mechanical stress modulates the geometric ionic transport pathways in the Li_6PS_5Cl medium.

4.11 | Dark Field X-Ray Microscopy (DFXM)

Dark field X-ray microscopy experiments were conducted at beamline ID03 [57] at the European Synchrotron Radiation Facility. A photon energy of 17 keV was selected using a channel-cut Si monochromator. Sample alignment was performed using a near-field detector positioned 40 mm downstream from the sample. After aligning the diffraction from individual powder grains, the diffracted beam was magnified using 87 2D Be CRLs positioned 275 mm from the sample. The magnified beam was captured on a far-field camera located 5113 mm downstream. The high-resolution imaging system consisted of a back-illuminated PCO camera coupled with a scintillator and a 10 × visible light objective. The effective pixel size on the detector, accounting for an −18.34 × X-ray magnification, was 36 nm/pixel. To investigate local orientation and strain around the *hkl* diffraction vector, the sample was rotated in a 2D mesh using tilt angles φ and χ, with a fixed 2θ of 12.05°. Measurements were conducted on two grains from the Li_6PS_5Cl–4 µm sample and Li_6PS_5Cl–11 µm sample. Typical scan ranges were <0.6° for ϕ with step sizes as fine as 0.001°. Data analysis was performed using the open-source software *darfix* [58].

In dark-field X-ray microscopy—similar to electron backscatter diffraction—geometrically necessary dislocation (GND) density was estimated from local orientation gradients across a crystalline volume. Orientation maps were typically obtained by fitting rocking curves (in ϕ and χ tilts) on a per-pixel basis around a selected Bragg reflection. The center of mass (COM) of the rocking curves represented the local lattice rotation, while the full-width at half-maximum (FWHM) could serve as a qualitative indicator of lattice distortion or defect content. To compute GND maps quantitatively, the spatial gradients of the COM orientation maps were used. Specifically, for a selected diffraction vector (220) (in this case for the argyrodite materials), the local misorientation angle $\Delta\theta$ per unit length was calculated using the combined spatial derivatives of the ϕ and χ COM maps,

$$\Delta\theta_{local} = \sqrt{(\Delta\phi^2 + \Delta\chi^2)} \tag{6}$$

Assuming a known Burgers vector magnitude, b, the misorientation across a subgrain grain could be used to estimate dislocation density via the relationship

$$\rho_{GND} = \frac{\Delta\theta_{local}}{b \cdot \text{effective pixel size}} \tag{7}$$

where $\Delta\theta_{local}$ was measured in radians per unit length (typically rad/m), and $[b]$ = m. This yields $[\rho_{GND}]$ = dislocations/m^{-2}. The resulting maps reflected lattice curvature and revealed the spatial distribution of dislocation content within grains [59, 60].

4.12 | Particle Size Distribution (PSD)

The volume-weighted particle size distribution was obtained by laser diffraction experiments using a HELOS particle size analyzer (Sympatec). For each sample, 4.5 mg of powder was dispersed into 4 mL of *p*-xylene mixture containing 1 wt.% polyisobutylene, which was added to enhance the viscosity. Subsequently, the dispersion was ultrasonicated with an ultrasonic finger for approximately 15 min in Ar atmosphere (H_2O <0.5 ppm, O_2 <0.1 ppm). To obtain a measurement, the dispersion was injected into a cuvette filled with 40 mL of *p*-xylene to 1 wt.% polyisobutylene mixture outside the glovebox until a sufficient optical saturation for a reliable measurement was achieved. The dispersion was stirred throughout the measurement to prevent sedimentation of particles.

Acknowledgements

The authors would like to acknowledge AMG Lithium for providing the solid electrolytes and the support of BMBF MaSSiF under project number 03XP0519C. We acknowledged Diamond Light Source for time on beamline I15 under proposal CY36607. J.K., O.M. and M.H. were members of the International Graduate School for Battery Chemistry, Characterization, Analysis, Recycling, and Application (BACCARA), which was funded by the Ministry for Culture and Science of North Rhine Westphalia, Germany. A.A.F., M.A., F.M.Z. and D.R. acknowledged the European Union's Horizon Europe research and innovation program under grant agreement no. 101069686 (PULSELiON). A.A.F. acknowledged the funding support of the French National Research Agency under the France 2030 program (Grant ANR-22-PEBA-0002, PEPR project "BATMAN"). A.A.F. acknowledged Institut Universitaire de France for the support. We thank ESRF for providing the beamtime at ID03. C.Y. acknowledged the financial support from the ERC Starting Grant nr 10116911. D.R. acknowledged financial support by the Austrian Federal Ministry for Digital and Economic Affairs, the National Foundation for Research, Technology and Development and the Christian Doppler Research Association (Christian Doppler Laboratory for Solid State Batteries). We thank Eva Schlautmann for her assistance with the SEM images.

Open access funding enabled and organized by Projekt DEAL.

Conflicts of Interest

The authors declare no conflicts of interest.

Data Availability Statement

The data that support the findings of this study have been archived at 10.17879/12978180830.

References

1. J. Janek and W. G. Zeier, "Challenges in Speeding up Solid-State Battery Development," *Nature Energy* 8 (2023): 230–240, https://doi.org/10.1038/s41560-023-01208-9.

2. T. Famprikis, P. Canepa, J. A. Dawson, M. S. Islam, and C. Masquelier, "Fundamentals of Inorganic Solid-State Electrolytes for Batteries," *Nature Materials* 18, no. 12 (2019): 1278–1291, https://doi.org/10.1038/s41563-019-0431-3.

3. S. Ohno, A. Banik, G. F. Dewald, et al., "Materials Design of Ionic Conductors for Solid State Batteries," *Progress in Energy* 2 (2020): 022001, https://doi.org/10.1088/2516-1083/ab73dd.

4. Y. Kato, S. Hori, T. Saito, et al., "High-Power All-Solid-State Batteries Using Sulfide Superionic Conductors," *Nature Energy* 1 (2016): 1–7, https://doi.org/10.1038/nenergy.2016.30.

5. S. Li, J. Lin, M. Schaller, et al., "High-Entropy Lithium Argyrodite Solid Electrolytes Enabling Stable All-Solid-State Batteries," *Angewandte Chemie International Edition* 62 (2023): 202314155, https://doi.org/10.1002/anie.202314155.

6. J. Sung, J. Heo, D.-H. Kim, et al., "Recent Advances in All-Solid-State Batteries for Commercialization," *Materials Chemistry Frontiers* 8 (2024): 1861–1887, https://doi.org/10.1039/d3qm01171b.

7. C. Schneider, C. P. Schmidt, A. Neumann, et al., "Effect of Particle Size and Pressure on the Transport Properties of the Fast Ion Conductor t-Li_7SiPS_8," *Advanced Energy Materials* 13 (2023): 2203873, https://doi.org/10.1002/aenm.202203873.

8. J.-M. Doux, Y. Yang, D. H. S. Tan, et al., "Pressure Effects on Sulfide Electrolytes for All Solid-State Batteries," *Journal of Materials Chemistry A* 8 (2020): 5049–5055, https://doi.org/10.1039/C9TA12889A.

9. Q. Tran, M. Agrawal, M. Häusler, et al., "Uni-Axial Densification of Slurry-Casted Li_6PS_5Cl Tapes: The Role of Particle Size Distribution and Densification Pressure," *Advanced Materials* 37 (2025): 2501592, https://doi.org/10.1002/adma.202501592.

10. S. Ohno, T. Bernges, J. Buchheim, et al., "How Certain Are the Reported Ionic Conductivities of Thiophosphate-Based Solid Electrolytes? An Interlaboratory Study," *ACS Energy Letters* 5 (2020): 910–915, https://doi.org/10.1021/acsenergylett.9b02764.

11. M. S. Diallo, T. Shi, Y. Zhang, et al., "Effect of Solid-Electrolyte Pellet Density on Failure of Solid-State Batteries," *Nature Communications* 15 (2024): 858, https://doi.org/10.1038/s41467-024-45030-7.

12. M. Kodama, S. Komiyama, A. Ohashi, N. Horikawa, K. Kawamura, and S. Hirai, "High-Pressure in Situ X-Ray Computed Tomography and Numerical Simulation of Sulfide Solid Electrolyte," *Journal of Power Sources* 462 (2020): 228160, https://doi.org/10.1016/j.jpowsour.2020.228160.

13. O. Korjus, S. Mitra, Q. Berrod, et al., "Investigating the Densification of Li_6PS_5Cl Solid Electrolyte Through Multi-Scale Characterization Techniques," *Energy Storage Materials* 82 (2025): 104589, https://doi.org/10.1016/j.ensm.2025.104589.

14. C. A. Heck, T. Scharmann, M. Osenberg, et al., "Opportunities and Challenges of Calendering Sulfide-Based Separators for Solid-State Batteries," *Batteries & Supercaps* 7 (2024): 202300487, https://doi.org/10.1002/batt.202300487.

15. M. Rosner, S. Cangaz, A. Dupuy, et al., "Toward Higher Energy Density All-Solid-State Batteries by Production of Freestanding Thin Solid Sulfidic Electrolyte Membranes in a Roll-to-Roll Process," *Advanced Energy Materials* 15 (2025): 2404790, https://doi.org/10.1002/aenm.202404790.

16. A. Dupuy, S. Cangaz, M. Rosner, et al., "Scalable Cathode Electrode and Sulfidic Separator Manufacturing by DRYtraec Process for Solid-State Batteries," *Journal of Energy Storage* 134 (2025): 118172, https://doi.org/10.1016/j.est.2025.118172.

17. M. So, G. Inoue, R. Hirate, K. Nunoshita, S. Ishikawa, and Y. Tsuge, "Effect of Mold Pressure on Compaction and Ion Conductivity of All-Solid-State Batteries Revealed by the Discrete Element Method," *Journal of Power Sources* 508 (2021): 230344, https://doi.org/10.1016/j.jpowsour.2021.230344.

18. T. Shi, Q. Tu, Y. Tian, et al., "High Active Material Loading in All-Solid-State Battery Electrode via Particle Size Optimization," *Advanced Energy Materials* 10 (2020): 1902881, https://doi.org/10.1002/aenm.201902881.

19. M. Alabdali, F. M. Zanotto, M. Chouchane, et al., "Understanding Mechanical Stresses upon Solid-State Battery Electrode Cycling Using Discrete Element Method," *Energy Storage Materials* 70 (2024): 103527, https://doi.org/10.1016/j.ensm.2024.103527.

20. J. Tippens, J. C. Miers, A. Afshar, et al., "Visualizing Chemomechanical Degradation of a Solid-State Battery Electrolyte," *ACS Energy Letters* 4 (2019): 1475–1483, https://doi.org/10.1021/acsenergylett.9b00816.

21. M. Kodama, A. Ohashi, and S. Hirai, "In Situ X-Ray Computational Tomography Measurement of Single Particle Behavior of Sulfide Solid Electrolyte Under High-Pressure Compression," *Journal of Power Sources Advances* 4 (2020): 100019, https://doi.org/10.1016/j.powera.2020.100019.

22. V. Faka, M. T. Agne, M. A. Lange, et al., "Pressure-Induced Dislocations and Their Influence on Ionic Transport in Li^+-Conducting Argyrodites," *Journal of the American Chemical Society* 146 (2024): 1710–1721, https://doi.org/10.1021/jacs.3c12323.

23. E. Schlautmann, A. Weiß, O. Maus, et al., "Impact of the Solid Electrolyte Particle Size Distribution in Sulfide-Based Solid-State Battery Composites," *Advanced Energy Materials* 13 (2023): 1–9, https://doi.org/10.1002/aenm.202302309.

24. S. Puls, E. Nazmutdinova, F. Kalyk, et al., "Benchmarking the Reproducibility of All-Solid-State Battery Cell Performance," *Nature Energy* 9 (2024): 1310–1320, https://doi.org/10.1038/s41560-024-01634-3.

25. C. Sun and D. J. W. Grant, "Influence of Elastic Deformation of Particles on Heckel Analysis," *Pharmaceutical Development and Technology* 6 (2001): 193–200, https://doi.org/10.1081/PDT-100000738.

26. V. Faka, M. T. Agne, P. Till, et al., "Pressure Dependence of Ionic Conductivity in Site Disordered Lithium Superionic Argyrodite Li_6PS_5Br," *Energy Advances* 2 (2023): 1915–1925, https://doi.org/10.1039/D3YA00424D.

27. T. Famprikis, Ö. U. Kudu, J. A. Dawson, et al., "Under Pressure: Mechanochemical Effects on Structure and Ion Conduction in the Sodium-Ion Solid Electrolyte Na_3PS_4," *Journal of the American Chemical Society* 142, no. 43 (2020): 18422–18436, https://doi.org/10.1021/jacs.0c06668.

28. M. U. Ghori, "Powder Compaction: Compression Properties of Cellulose Ethers," *British Journal of Pharmacy* 1 (2016): 19–29, https://doi.org/10.5920/bjpharm.2016.09.

29. J. Tu, X. Wang, and B. Liu, "Fragmentation Behavior of Diamond Particles With Different Particle Size and Ratio Under High Pressure Compaction," *Ceramics International* 50 (2024): 36145–36155, https://doi.org/10.1016/j.ceramint.2024.06.428.

30. H. Xie, F. Deng, X. Yang, and S. Han, "Study of Fragmentation in CBN Powders Under Ultra-High Pressure," *Ceramics International* 46 (2020): 1631–1639, https://doi.org/10.1016/j.ceramint.2019.09.135.

31. H. J. Deiseroth, S. T. Kong, H. Eckert, et al., "Li_6PS_5X: A Class of Crystalline Li-Rich Solids with an Unusually High Li+ Mobility," *Angewandte Chemie* 2008, 47, 767–770, https://doi.org/10.1002/anie.200703900.

32. C. Yildirim, F. Flatscher, S. Ganschow, et al., "Understanding the Origin of Lithium Dendrite Branching in $Li_{6.5}La_3Zr_{1.5}Ta_{0.5}O_{12}$ Solid-State Electrolyte via Microscopy Measurements," *Nature Communications* 15 (2024): 1–8, https://doi.org/10.1038/s41467-024-52412-4.

33. C. Yildirim, H. F. Poulsen, G. Winther, C. Detlefs, P. H. Huang, and L. E. Dresselhaus-Marais, "Extensive 3D Mapping of Dislocation Structures in Bulk Aluminum," *Scientific Reports* 13 (2023): 3834, https://doi.org/10.1038/s41598-023-30767-w.

34. F. Radjai, "Modeling Force Transmission in Granular Materials," *Comptes Rendus Physique* 16 (2015): 3–9, https://doi.org/10.1016/j.crhy.2015.01.003.

35. J. Janek and W. G. Zeier, "A Solid Future for Battery Development," *Nature Energy* 1 (2016): 1–4, https://doi.org/10.1038/nenergy.2016.141.

36. S.-H. Yu, X. Feng, N. Zhang, J. Seok, and H. D. Abruña, "Understanding Conversion-Type Electrodes for Lithium Rechargeable Batteries," *Accounts of Chemical Research* 51 (2018): 273–281, https://doi.org/10.1021/acs.accounts.7b00487.

37. S. Ohno and W. G. Zeier, "Toward Practical Solid-State Lithium–Sulfur Batteries: Challenges and Perspectives," *Accounts of Materials Research* 2 (2021): 869–880, https://doi.org/10.1021/accountsmr.1c00116.

38. H. Huo and J. Janek, "Silicon as Emerging Anode in Solid-State Batteries," *ACS Energy Letters* 7 (2022): 4005–4016, https://doi.org/10.1021/acsenergylett.2c01950.

39. R. W. Heckel, "An Analysis of Powder Compaction Phenomena," *Transactions of the Metallurgical Society of AIME* 221 (1961): 1001–1008.

40. C. Prescher and V. B. Prakapenka, "DIOPTAS: A Program for Reduction of Two-Dimensional X-Ray Diffraction Data and Data Exploration," *High Pressure Research* 35 (2015): 223–230, https://doi.org/10.1080/08957959.2015.1059835.

41. A. A. T. Coelho, "TOPAS and TOPAS-Academic: An Optimization Program Integrating Computer Algebra and Crystallographic Objects Written in C++," *Journal of Applied Crystallography* 51 (2018): 210–218, https://doi.org/10.1107/S1600576718000183.

42. S. Klotz, J.-C. Chervin, P. Munsch, and G. Le Marchand, "Hydrostatic Limits of 11 Pressure Transmitting Media," *Journal of Physics D: Applied Physics* 42 (2009): 075413, https://doi.org/10.1088/0022-3727/42/7/075413.

43. R. J. Angel, M. Bujak, J. Zhao, G. D. Gatta, and S. D. Jacobsen, "Effective Hydrostatic Limits of Pressure Media for High-Pressure Crystallographic Studies," *Journal of Applied Crystallography* 40 (2007): 26–32, https://doi.org/10.1107/S0021889806045523.

44. H. K. Mao, J. Xu, and P. M. Bell, "Calibration of the Ruby Pressure Gauge to 800 kbar Under Quasi-Hydrostatic Conditions," *Journal of Geophysical Research: Solid Earth* 91 (1986): 4673–4676, https://doi.org/10.1029/jb091ib05p04673.

45. K. R. P. Syassen, "High Pressure Studies Of Superconductivity," *High Pressure Research* 28 (2008): 75–126, https://doi.org/10.1080/08957950802235640.

46. G. Williamson and W. Hall, "X-Ray Line Broadening From Filed Aluminium and Wolfram," *Acta Metallurgica* 1 (1953): 22–31, https://doi.org/10.1016/0001-6160(53)90006-6.

47. M. A. Kraft, S. P. Culver, M. Calderon, et al., "Influence of Lattice Polarizability on the Ionic Conductivity in the Lithium Superionic Argyrodites Li_6PS_5X (X = Cl, Br, I)," *Journal of the American Chemical Society* 139 (2017): 10909–10918, https://doi.org/10.1021/jacs.7b06327.

48. S. Christensen, N. Bindzus, M. Sist, M. Takata, and B. B. S. D. Iversen, "Structural Disorder, Anisotropic Micro-Strain and Cation Vacancies in Thermo-Electric Lead Chalcogenides," *Physical Chemistry Chemical Physics* 18 (2016): 15874–15883, https://doi.org/10.1039/C6CP01730D.

49. R. Hanus, M. T. Agne, A. J. E. Rettie, et al., "Lattice Softening Significantly Reduces Thermal Conductivity and Leads to High Thermoelectric Efficiency," *Advanced Materials* 31 (2019): 1900108, https://doi.org/10.1002/adma.201900108.

50. P. W. Stephens, "Phenomenological Model of Anisotropic Peak Broadening in Powder Diffraction," *Journal of Applied Crystallography* 32 (1999): 281–289, https://doi.org/10.1107/S0021889898006001.

51. B. H. Toby and R. B. Von Dreele, "GSAS-II: The genesis of a Modern Open-Source all Purpose Crystallography Software Package," *Journal of Applied Crystallography* 46 (2013): 544–549, https://doi.org/10.1107/S0021889813003531.

52. P. Juhás, T. Davis, C. L. Farrow, and S. J. L. Billinge, "PDFgetX3: A Rapid and Highly Automatable Program for Processing Powder Diffraction Data Into Total Scattering Pair Distribution Functions," *Journal of Applied Crystallography* 46 (2013): 560–566, https://doi.org/10.1107/S0021889813005190.

53. R. C. Howell, T. Proffen, and S. D. Conradson, "Pair Distribution Function and Structure Factor of Spherical Particles," *Physical Review B* 73 (2006): 094107, https://doi.org/10.1103/PhysRevB.73.094107.

54. C. Kloss, C. Goniva, A. Hager, S. Amberger, and S. M. Pirker, "Models, Algorithms and Validation for Opensource DEM and CFD-DEM," *Progress in Computational Fluid Dynamics, An International Journal* 12 (2012): 140–152, https://doi.org/10.1504/PCFD.2012.047457.

55. J. Xu, B. Paredes-Goyes, Z. Su, et al., "Computational Model for Predicting Particle Fracture During Electrode Calendering," *Batteries & Supercaps* 6 (2023): 202300371, https://doi.org/10.1002/batt.202300371.

56. Math2Market GmbH, *GeoDict Simulation Software* (2023), https://doi.org/10.30423/release.geodict2023.

57. H. Isern, T. Brochard, T. Dufrane, et al., "The ESRF Dark-Field X-Ray Microscope at ID03," *Journal of Physics: Conference Series* 3010 (2025): 012163, https://doi.org/10.1088/1742-6596/3010/1/012163.

58. J. Garriga Ferrer, R. Rodríguez-Lamas, H. Payno, et al., "Darfix—Data Analysis for Dark-Field X-Ray Microscopy," *Journal of Synchrotron Radiation* 30 (2023): 527–537, https://doi.org/10.1107/S1600577523001674.

59. C. Yildirim, N. Mavrikakis, P. K. Cook, et al., "Multiscale Exploration of Texture and Microstructure Development in Recrystallization Annealing of Heavily Deformed Ferritic Alloys," *IOP Conference Series: Materials Science and Engineering* 1249 (2022): 012044, https://doi.org/10.1088/1757-899x/1249/1/012044.

60. Y. Chen, Y. T. Tang, D. M. Collins, et al., "High-Resolution 3D Strain and Orientation Mapping Within a Grain of a Directed Energy Deposition Laser Additively Manufactured Superalloy," *Scripta Materialia* 234 (2023): 115579, https://doi.org/10.1016/j.scriptamat.2023.115579.

Supporting Information

Additional supporting information can be found online in the Supporting Information section.

Supporting File: aenm70650-sup-0001-SuppMat.pdf.